Experimental and Numerical Investigation into Hydraulic Fracture and Natural Fracture Interaction in Shale Formations

Yildirim, B., Durucan, S., Cao, W., Cai, W., Shi, J., Korre, A.

Department of Earth Science and Engineering, Royal School of Mines, Imperial College London, London SW7 2AZ, United Kingdom.

Wolf, K-H.

Department of Geoscience and Engineering, Delft University of Technology, Delft, the Netherlands

ABSTRACT: Two 0.3 m × 0.3 m × 0.3 m shale blocks, one representing a homogeneous sample while the other representing a naturally fractured sample, are modelled using the lattice based DEM code, XSite. The synthetic rock mass approach (SRM), which assigns the smooth joint contacts (SJM) to the weakness planes, is used to represent the natural fractures in shale block-2. Firstly, the developed models are compared with the findings of previously conducted true-triaxial hydraulic fracturing experiments with acoustic measurements, and their subsequent computed tomography (CT) and seismic velocity tomography results. The 3D model results confirmed the curved shape hydraulic fractures, which propagated perpendicular to the minimum stress directions in both shale blocks. Model results also captured the natural fracture (NF) and hydraulic fracture (HF) interaction, particularly the arrest, the dilation of major NFs, followed by crossing with offset mechanism, in shale block-2. Secondly, the parametric studies are carried out to investigate the role of fluid flow rate (q), and fluid viscosity (μ) on different NF/HF interaction mechanisms. The effects of q and μ are discussed based on the total stimulated area including the tensile and shear microcracks, the pipe apertures, and the pressure evolutions within NFs.

1 INTRODUCTION

Presence of natural fractures (NF) is critical in defining a prospective shale gas play. The well-known gas shale plays which have contributed significantly to natural gas production in the United States are usually the naturally fractured reservoirs, in which the opening-mode of fractures enhance the production by increasing the treatment zone. The positive roles of natural fractures are explained as enhancing the reservoir permeability and the productivity in the case of open NFs, and increasing the fracture network complexity and the stimulated reservoir volume regardless of whether they are open or closed prior to fracture treatment (Li, 2014). On the other hand, a few researchers have indicated that the presence of NFs might be detrimental in gas production from shale plays (Walton and McLennan, 2013). To this end, a detailed analysis of NF and hydraulic fracture (HF) interaction mechanisms should be considered in the evaluation of naturally fractured unconventional reservoirs' productivity.

Previous research investigated the effects of different parameters on the NF/HF interaction mechanisms, particularly the direct crossing, arresting, and offsetting scenarios (Beugelsdijk et al., 2000; Nagel et al., 2011; Chuprakov et al., 2013; Kresse et al., 2013; Wu and Olson, 2014; Mikada and Takekawa, 2015; Yoon et al., 2017; Zhou et al, 2017). These studies suggested that the effects of in-situ stress state, natural fractures, and the treatment parameters are significant in controlling the HF propagation path and the corresponding NF/HF interactions.

Despite the large amount of experimental and numerical modelling research conducted, the performance of HFs in naturally fractured structures and their effect on hydrocarbon production is still not well understood. To this end, this research aimed at developing a better understanding of NF/HF interaction and its impact on fracture network properties created in shale formations by three-dimensional lattice based discrete element modelling (DEM) approach, compared with the large-scale hydraulic fracturing experiments. As reported earlier in Yildirim et al. (2018) true-triaxial hydraulic fracturing experiments with acoustic measurements were initially carried out on one homogenous shale and one naturally fractured coal block of 0.3 × 0.3 m × 0.3 m cubic samples. These experiments were recently complemented with another experiment on a second shale block, which contains four visible NF planes. Both fracturing tests on the two shales were conducted under the same experimental conditions, and the stress, displacement, borehole pressure, and seismic response were recorded

during the fluid injection process. Furthermore, computed tomography (CT) and seismic velocity tomography analyses were performed and the results were evaluated for further identification of location and geometry of the hydraulic and the natural fractures in the two shale blocks. The first part of this paper presents a detailed analysis and comparison of the mechanisms involved in these two experiments. Subsequently, two 3D DEMs, one representing the homogeneous sample while the other representing the naturally fractured sample, are constructed to simulate the fracturing behaviour observed in these experiments. The model findings are compared with the results of hydraulic fracturing experiments, and their corresponding CT scan and seismic velocity tomography analyses. Parametric studies carried out investigated the role of controllable treatment parameters, particularly the fluid flow rate (q), and fluid viscosity (μ), on different NF/HF interaction mechanisms. The quantification of fracture network development is represented by the total stimulated area consisting of the tensile and shear microcracks, the pressure evaluation within NFs, and the aperture of pipes as the fluid flow conduits within the model. The second part of this paper presents the findings of these numerical studies.

2 EXPERIMENTAL RESEARCH

2.1 Sample Preparation and Experimental Procedure

The shale samples used in this research were collected from the Hope Cement Works shale quarry in Derbyshire, UK, and were first characterised through several geomechanical tests (Table 1).

Table 1 Mechanical, elastic, and flow properties of Derbyshire Shale.

UCS (MPa)	81.69
Tensile strength (MPa)	8.99
Young's Modulus (GPa)	15.38
Poisson's ratio	0.269
Porosity (%)	1.88
Permeability (m^2)	9.86e-17

A 23 mm hole was drilled through the YD and ZC faces of shale block 1 and shale block-2 respectively. Shale block-1 was drilled through the middle of the sample whereas shale sample-2 was drilled collaterally and 8 cm away from the main natural fracture (NF1) in order to ensure NF/HF interaction. A 15 cm long casing was used without leaving an open hole in both samples (Figure 1).

The details of true-triaxial testing system used at TU Delft Geoscience Laboratory can be found in Yildirim et al. (2018). The acoustic measurement system consists of 960 source-receiver pairs including the P-wave and S-wave straight transmission (stP, stS), oblique transmission (otP, otS), and diffraction (dP, dS) pairs (Figure 2).

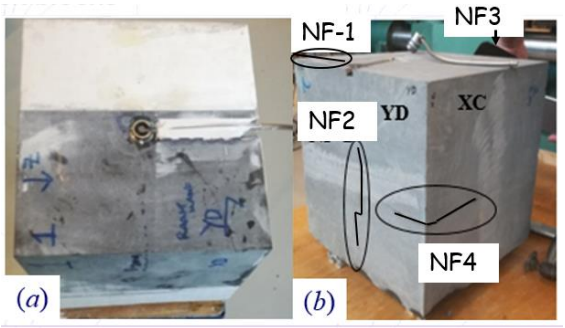

Figure 1 Prepared samples: (a) homogeneous shale block-1, and (b) naturally fractured shale block-2.

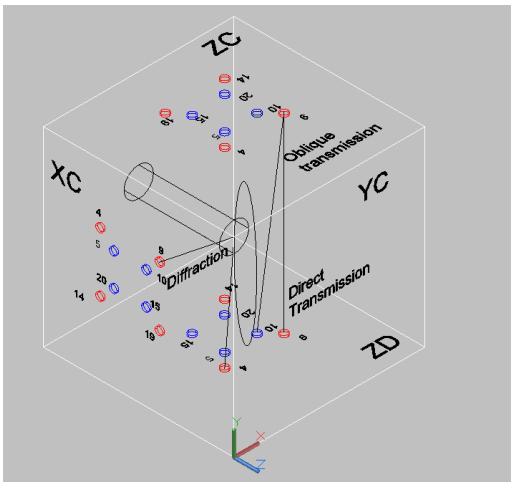

Figure 2 Seismic wave raypaths.

First, the seismic wave profiles under different confinements were obtained implementing a stepwise loading procedure before the hydraulic fracturing experiments. The results proposed a slight increase in seismic wave velocities with increasing confining pressure. This result is mainly correlated with the further closure of the comparatively open NFs, microcracks, and pores under higher confining pressures. However, despite the presence of NFs in shale block-2, seismic wave velocities were found to be in the similar range with those of the shale block-1, which may indicate that the NFs were either closed or cemented so that they did not have a significant effect on the seismic wave profiles.

Next, the hydrofracturing experiments with acoustic measurements were conducted applying the procedure explained earlier in Yildirim et al. (2018). To summarise, equal load was applied on each side of the cubes until the final stress state of 5MPa is reached. At the final stress level, stress magnitude in the x direction was decreased to 4MPa while keeping stress constant in y and z directions to induce a vertical fracture. The viscous silicon oil was injected at a constant flow rate of 1 ml/min. During the fluid injection stage, the load, pump pressure and seismic response were recorded. The initiation of the induced fracture could be detected by observing the changes in the acoustic measurement data, in particular the increase in amplitude and time delays in the propagation of seismic

waves. Once the fractures are induced, the samples were unloaded following the same stress stages used for the loading case. The samples were then taken out of the true-triaxial cell to observe the induced fractures by naked eye.

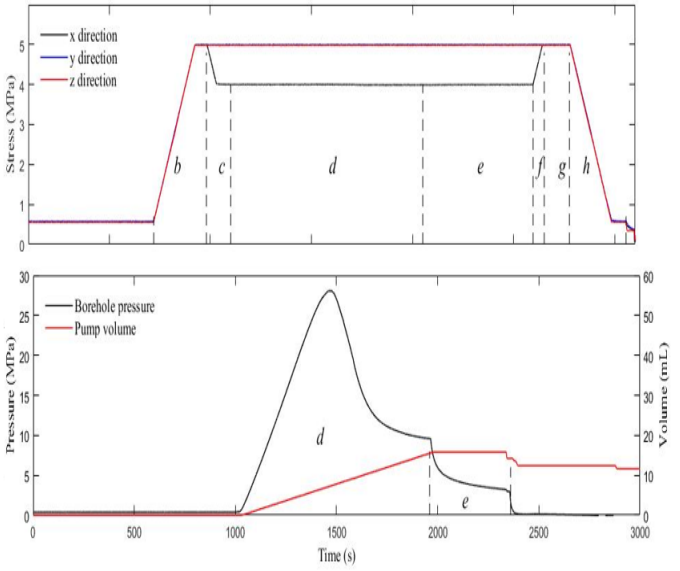

(a)

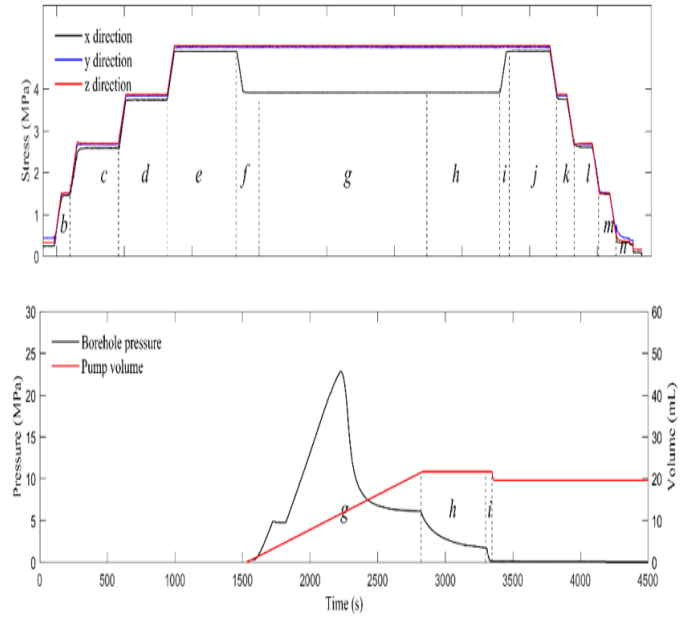

(b)

Figure 3 Stress, borehole pressure and volume responses of (a) shale block-1, and (b) shale block-2.

2.2 *Stress and Hydraulic Fracturing Response under Deviatoric Stress Conditions*

Borehole pressure data is one of the main indicator of the fracture initiation. In this context, the load and pump data were recorded and interpreted to evaluate the fracture initiations in both shale blocks. Fractures were believed to be induced when the borehole pressures reached their peaks and experienced sudden decrease, which occurred at 27.8 MPa fluid pressure, 495s after the injection for shale block-1, and at 22.8 MPa pressure at 650 s after the injection for shale block-2. Although it took similar time for fracture initiations in both samples, comparatively lower borehole pressure was recorded for HF generation in naturally fractured shale block-2. On the other hand, shale block-2 received a higher volume of silicon oil, which may indicate the oil infiltration into the natural fractures via the possible NF/HF interactions (Figure *3*).

2.3 *Acoustic Measurement Results*

In contrast to the seismograms of homogeneous shale block-1, the results of naturally fractured shale block-2 was found to be scattered due to additional reflections and diffractions, which required additional processing. When the original seismograms of shale block-1 and the processed seismograms of shale block-2 were evaluated, both the P wave and S wave transmission and diffraction pairs provided information on HF initiation. Observable changes in spectrograms were identified at 22nd scan in shale block-1 (Figure 4a), which corresponds to 660 seconds after injection. The changes in shale block-2 spectrograms, on the other hand, started at 45th scan (Figure 4b), which corresponds to 540 seconds after fluid injection.

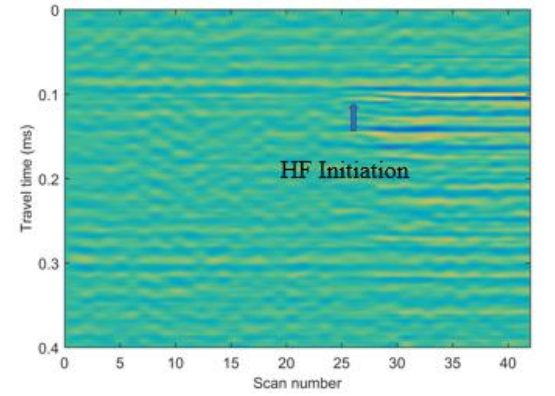

(a)

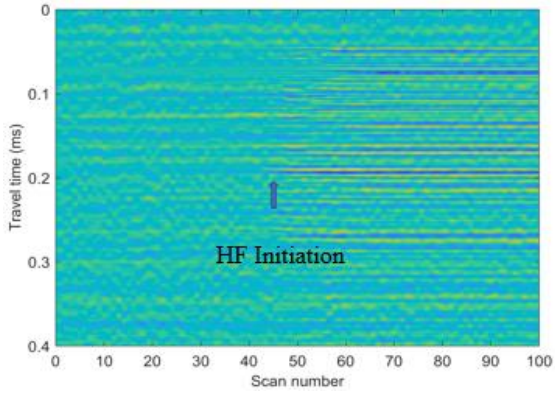

(b)

Figure 4 Spectrograms of diffraction pairs: (a) ZC19-C19 for shale block-1, and (b) ZC19-XD9 for shale block-2.

The acoustic results of both shale samples were found to be consistent with the pump data (Figure 3), which verifies that the induced fracture and fracturing fluid

interfere with the propagation of both the stS and stP seismic waves and influence seismic characteristics. On the other hand, as the secondary signals observed for the diffraction signals were not found to be promising, no clear indication of NF/HF interaction could be obtained from the acoustic monitoring of shale block-2.

2.4 Computed Tomography (CT) and Seismic Velocity Tomography Results

Considering the induced fracture orientation, post-fractured shale sample-1 was split into four blocks for the CT scan analysis. One of the split blocks, which included the wellbore, was further split into two pieces, which clearly show the induced fracture initiation at the wellbore and its propagation perpendicular to the minimum stress direction, which was confirmed by CT scan analysis (Figure 5). Similarly, the shale sample-2 was split into three smaller blocks after the fracturing experiment. Visualisation of the split shale block-2 suggested the HF/NF1 interaction and fluid leakage into NF1, followed by crossing with offset mechanism (Figure 6a).

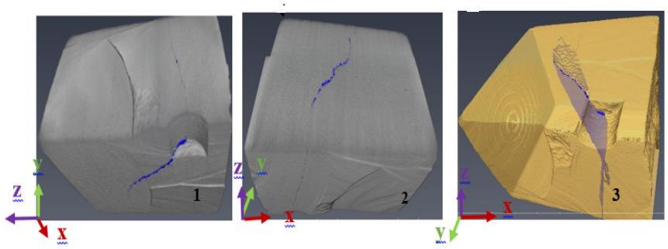

Figure 5 CT scan analysis of post hydrofractured and split shale-1 block and the curvature of the induced fracture.

The split block 2 was then placed into CT scanner which helped visualise the natural fractures, particularly the NF1 and NF2 (Figure 6b). In order to develop a better understanding of the HF propagation and its interaction with the NFs, further CT scanning sessions are planned using the split block 3. Seismic velocity tomography results (Figure 7) also confirmed the estimated HF propagations in both shale blocks based on the difference in the seismic wave velocities for the pre- and post-injection stages.

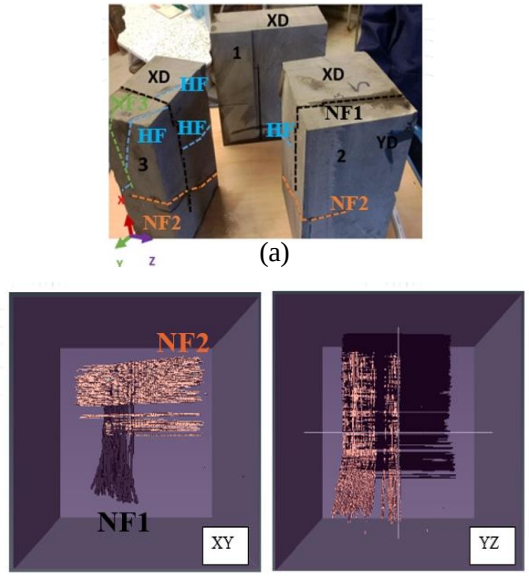

Figure 6. (a) Split shale block-2, and (b) CT scan results of 2nd piece.

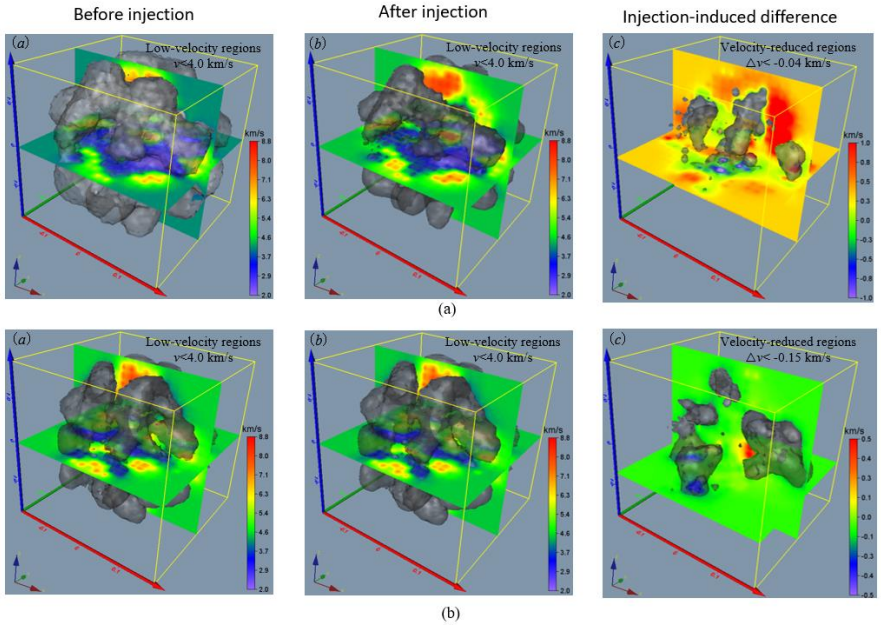

Figure 7. Seismic velocity tomography results: (a) Shale block-1, and (b) shale block-2.

3 NUMERICAL MODELLING RESEARCH

3.1 Lattice methodology

The XSite code, based on the distinct element modelling (DEM) approach, uses an explicit solution scheme by which the non-linear behaviour as fracturing, slip, opening/closure of joints can be well- represented. The lattice methodology used by XSite is a simplified version of the bonded particle model (BPM), in which the rock is modelled as circular (2D) or spherical (3D) particles connected at their contact points. In 3D lattice representation of brittle rock, the spherical particles in BPM are replaced by the point mass nodes, which are connected by non-linear springs (Damjanac et al., 2011). A 0.3m×0.3m×0.3m size lattice model of the laboratory tested samples with 0.015 m model resolution (particle size) is presented in Figure 8a. Simulation is carried out solving the equations of motion and force-displacement law applied to all nodes and all springs in the model respectively.

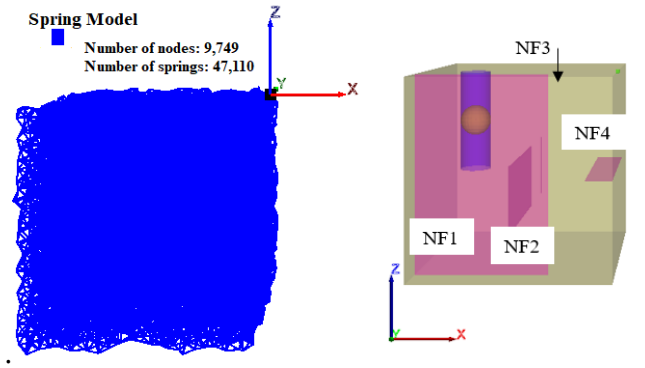

(a) (b)

Figure 8 (a) The spring model, and (b) the model features including rock, borehole, cluster, and weakness planes.

3.2 Fluid flow modelling in joints

The fluid flow in the rock matrix and in joints is solved differently (Damjanac et al, 2011; Damjanac et al., 2013). Due to low permeable nature of the shale, matrix flow is not activated through the simulations. The model uses the lubrication equation to simulate the flow within a fracture as a function of the aperture.

$$q = \beta k_r \frac{a3}{12\mu} / [p^A - p^B + \rho w g (z^A - z^B)]$$

Where a is hydraulic aperture, μ is viscosity of the fluid, p^A and p^B are fluid pressures at nodes "A" and "B" respectively, z^A and z^B are elevations of nodes "A" and "B" respectively

Dimensionless parameter β, which is a calibration parameter as a function of resolution, is used to match conductivity of a pipe network to the conductivity of a joint represented by parallel plates with aperture a. The relative permeability is given as a function of saturation as follows:

$$k_r = s^2(3 - 2s)$$

When the pipe is saturated, s is 1 and so the relative permeability is 1. The pressure increment, ΔP, during the flow timestep, Δt, is calculated as:

$$\Delta P = \frac{Q}{V} K_F \Delta t f$$

where K_F is the apparent bulk modulus, V is the node volume, and Q is the sum of all flow rates, q_i, from the pipes connected to the node (positive in the case of inflow):

$$Q = \sum qi$$

The model implements a full hydro mechanical coupling scheme, where the fracture permeability depends on the deformation of the solid model and the deformation and strength of the solid model depend on the fluid pressure.

The synthetic rock mass approach (SRM) is implemented in the code, in which the NFs are modelled by the modified smooth joint model (SJM). Four rectangular shape NFs fractures, all having 0.0001m aperture size, were implemented into model to simulate the naturally fractured shale block-2 (Figure 8b). The mechanical properties for the NFs, particularly the cohesion, tensile strength, friction angle, dilation angle, and normal and shear stiffnesses were all assigned to be zero, as the NFs are assumed to be very weak.

3.3 Comparison of the Numerical Model Results with the Experimental Observations

Two 0.3m×0.3m×0.3m size DEMs, one representing the homogeneous and the other representing the naturally fractured shale samples, were developed using XSite. The tensile and shear strengths of springs, which controls the macroscopic strength of the model, are calibrated according to the mechanical, elastic, and flow properties presented in Table 1. In-situ stress magnitudes were arranged according to the experimental procedure presented in section 2.1. All simulations were conducted for 20 seconds of fluid injection time.

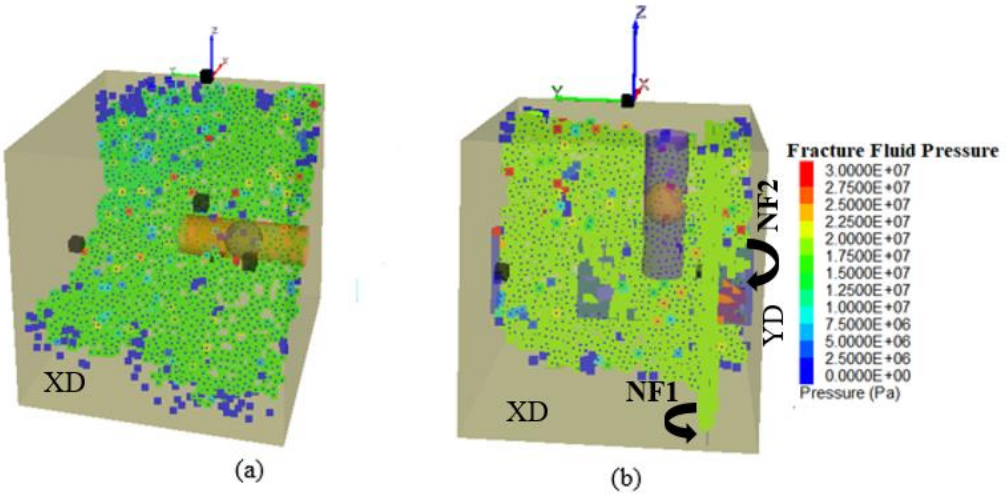

Figure 9 Numerical model results (a) shale block-1, and (b) shale block-2.

Figure 9 presents the numerical modelling results through the hydrofracturing experiments of shale-block-1 and shale block-2 respectively. Figure 9(*a*) indicates a curved shape fracture, which propagated perpendicular to the minimum horizontal stress direction (x). This result agrees well with the split shale block-1 images and its corresponding CT scan analysis results (Figure 5). The numerical modelling results of shale block-2 (Figure 9 (b)), on the other hand, indicates a vertically propagating HF, which is first arrested by the main natural fracture, NF1, and then by the secondary natural fracture NF2, in the model. An additional offset mechanism is observed after interacting with the NF2. Split shale block-2 images (Figure 6a) clearly confirm the arrest of propagating HF by NF1, followed by crossing with offset mechanisms, which is planned to be studied further by CT scan analysis of split shale block-2.

It should be noted that the random or stochastic arrangement of bonded-particle assembly used in the discrete element modeling technique brings out randomness in the curvature obtained under certain conditions, in particular when the modelled block is under low differential stresses. This, in fact, is more representative of the experimental conditions, as observed from the curvature of the induced fracture in the homogeneous shale block-1 (Figure 9a). It is believed that a distinctive increase in the stress ratio will decrease the curvature observed in the fracture propagation paths.

3.4 Parametric Research on Role of Flow Rate, and Fluid Viscosity

After the comparison of numerical model results and the experimental research observations, the effects of fluid flow rate (q) and viscosity (μ) on HF propagation and the subsequent NF/HF interactions in shale block-2 were investigated based the total stimulated reservoir area, pipe aperture, and the fluid pressure evolution in NFs.

Effect of fluid flow rate

In order to investigate the effects of q on HF propagation and NF/HF interaction, the q values were varied within the range $1e^{-3}$-$1.6e^{-2}$ litre/s while keeping the other variables constant.

Figure 10 presents the number of microcracks, the stimulated area including tensile microcracks, and the total stimulated area including both tensile and shear microcracks based on q. Results have suggested a logarithmic relationship between q and the stimulated reservoir area and the total number of microcracks, where the rate of increase in the total stimulated area is higher for lower q values, while it approaches a constant value at higher q values.

Figure 11 presents the pipe aperture distributions based on q. Results have suggested that higher q values lead to a more connected fluid network as both the number of pipes and their apertures increase with increasing flow rate.

Pressure within natural fractures are also presented in Figure 12, which suggests a similar pressure evolution trend for the major fractures NF1 and NF2, which are expected to interact with the HF. Lower q ($1e^{-3}$- $2e^{-3}$ l/s) values resulted in dilation of NF1 and NF2, while no change occurred for the minor NF3, and NF4. Higher q values, on the other hand, led to significant increase in the rate of pressure evolution within all NFs.

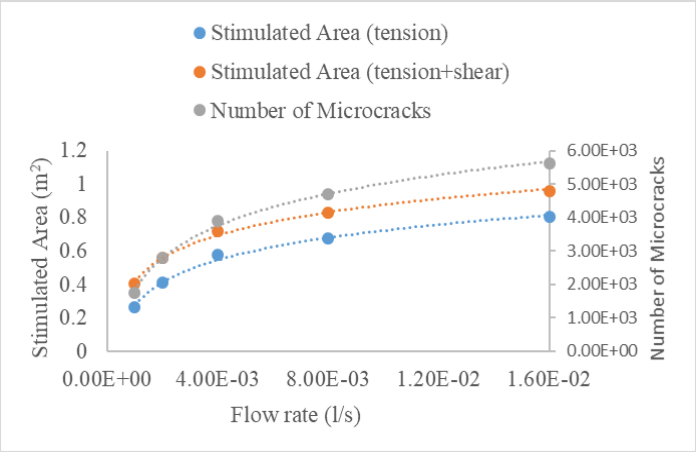

Figure 10 Number of microcracks and stimulated reservoir area based on flow rate.

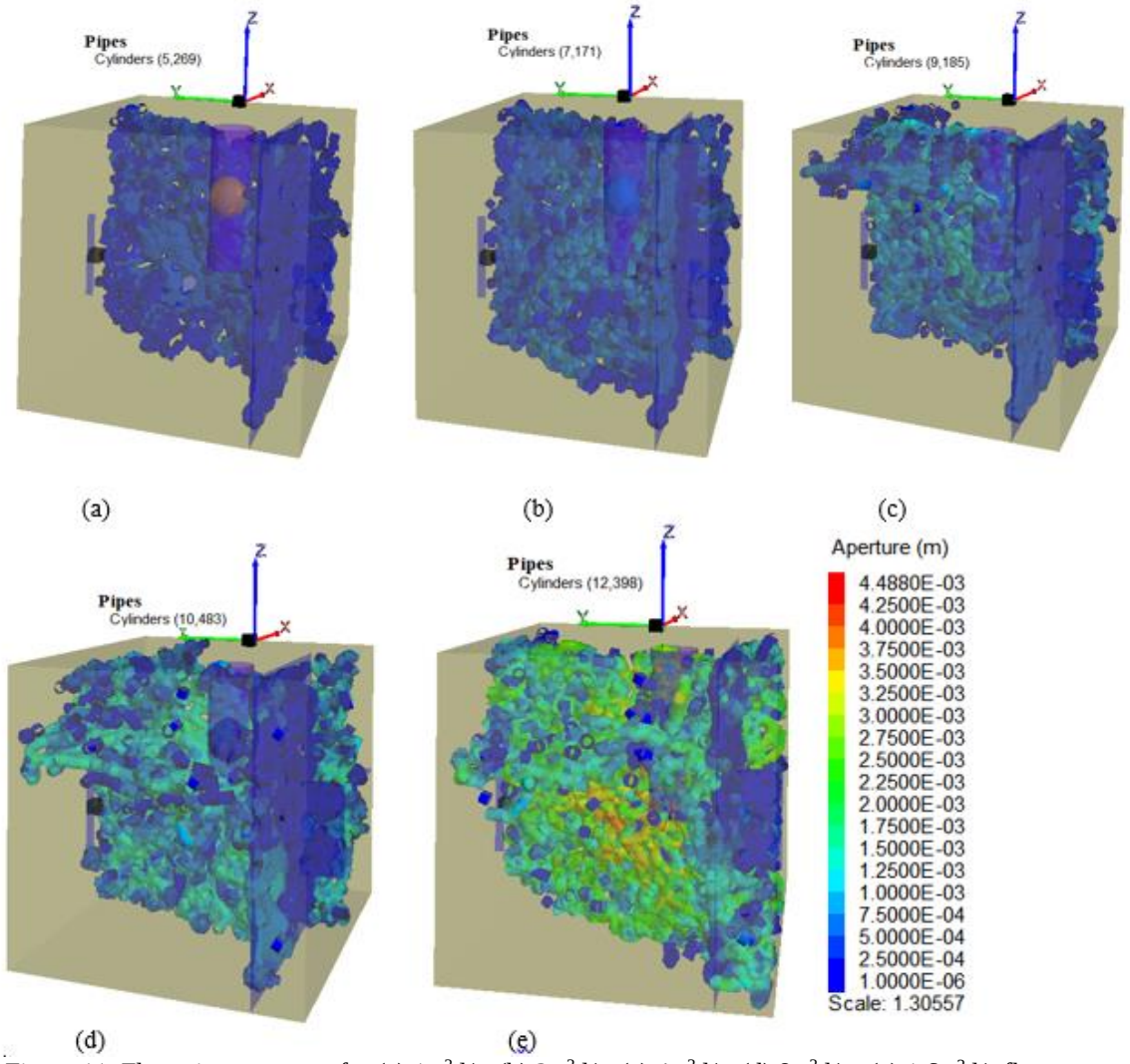

Figure 11. Flow pipe apertures for (a) $1e^{-3}$ l/s, (b) $2e^{-3}$ l/s. (c) $4e^{-3}$ l/s, (d) $8e^{-3}$ l/s., (e) $1.6e^{-2}$ l/s flow rate.

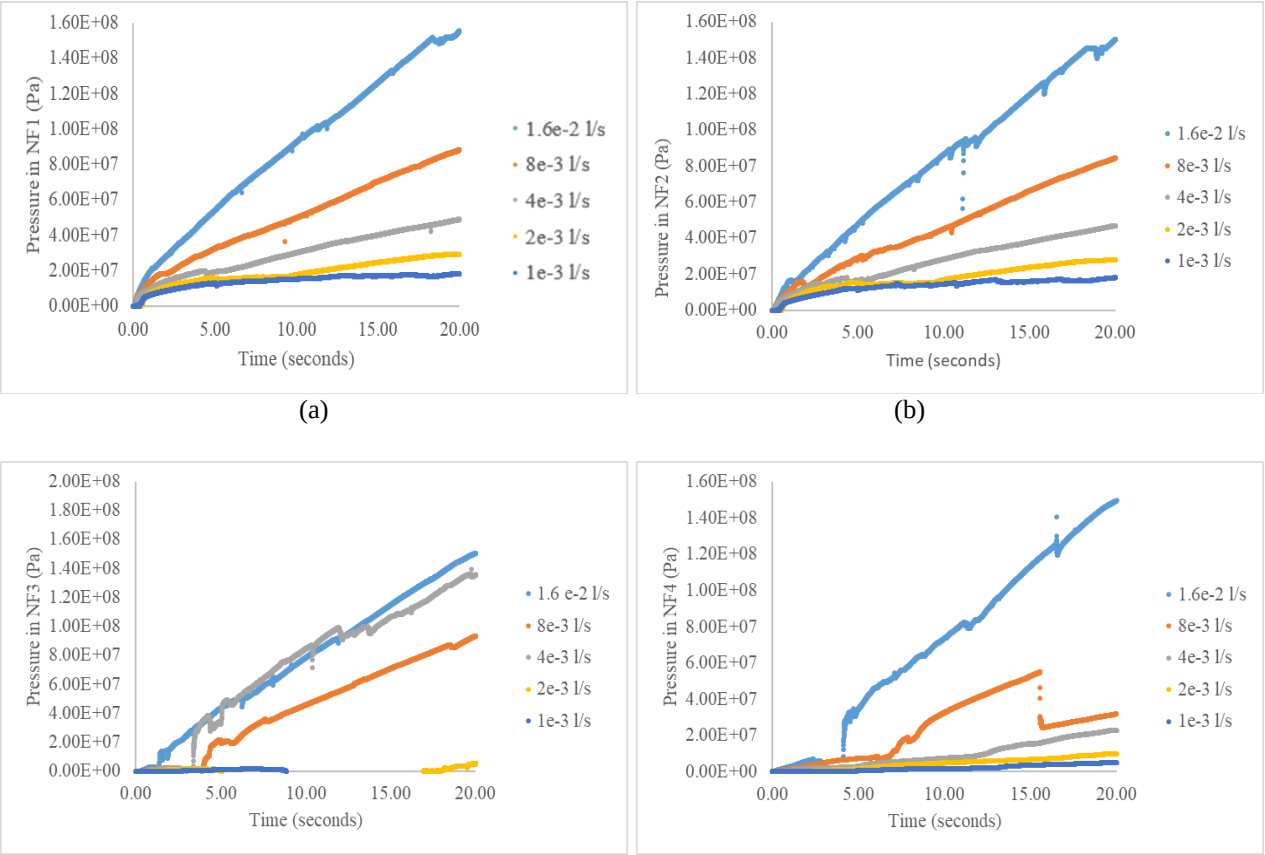

Figure 12 Pressure evolution in NFs (a) NF1, (b) NF2, (c)NF3, and (d) NF4

Effect of fluid viscosity

In order to investigate the effects of fluid viscosity (μ) on HF propagation and NF/HF interactions, the fluid flow rate (q) is kept constant at $1e^{-3}$ l/s while μ is changed within the range 0.05-0.5Pa·s. No significant difference was noted using the lower μ fluids (0.05 Pa·s and 0.10 Pa·s), while the higher μ fluids suggested the highest number of the induced microcracks and the widest total stimulated area at the end of 20 seconds (Figure 13a). The evolution of total stimulated area within 5 seconds of simulation is plotted and presented in Figure 13b.

Results clearly indicate that the rate of increase in total stimulated area is higher for a more viscous fluid (0.5 Pa·s) in the early stages of fracturing, after which the effect of μ decreases and the results of 0.24, 0.35, and 0.5 Pa·s converge on the same value.

The pipe aperture results (Figure 14), on the other hand, suggested the widest pipe aperture distribution around the borehole for the less viscous fluids. This can be due to the ease of local pressure increase by the lower μ fluid, while the effect of high μ fluid emerges in longer distances.

Considering that the effect of μ is more obvious in the early stages, the pressure evolution within NFs are also presented for the first 5 seconds of the simulation (Figure 15).

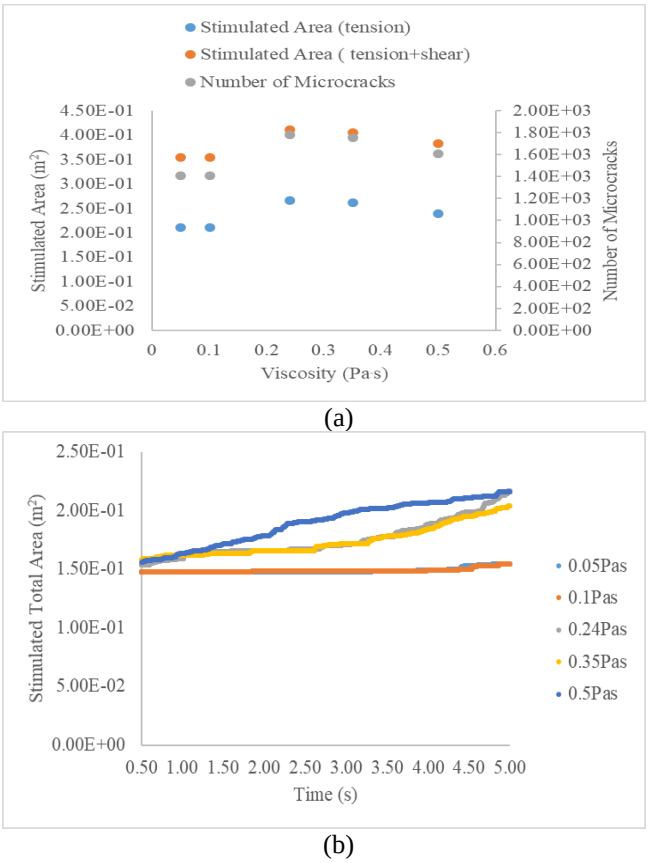

Figure 13 Stimulated reservoir area based on fluid viscosity (a) after 20seconds, (b) its evolution within 5 seconds.

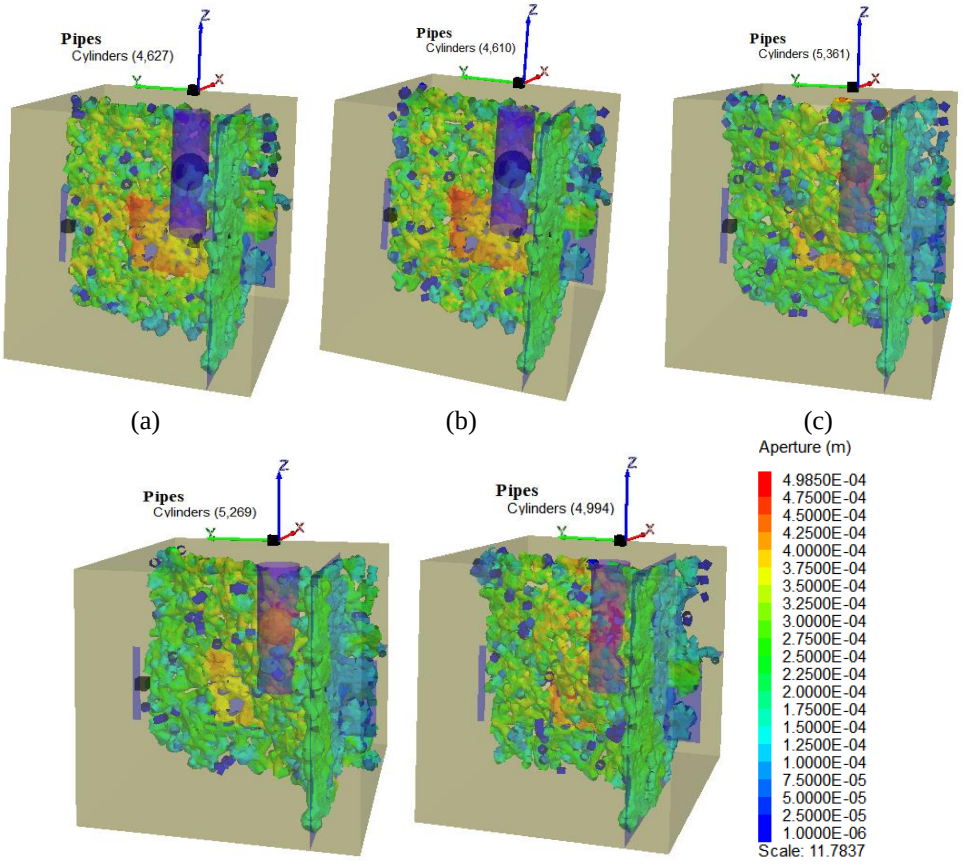

Figure 14 Flow pipe apertures at (a) 0.05Pa, (b) 0.1Pa. (c) 0.24Pa, (d) 0.35Pa, and (e) 0.5Pa viscosity.

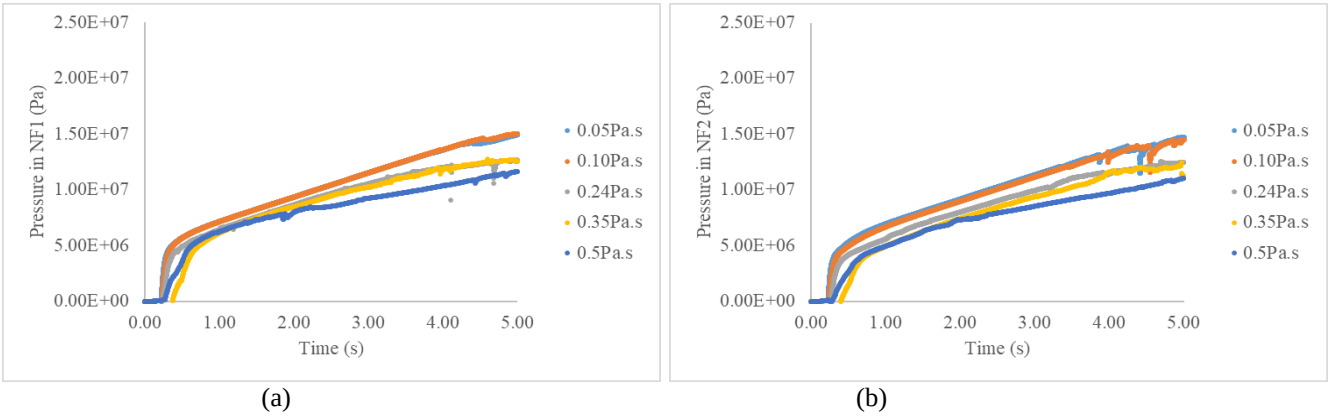

Figure 15 Pressure evolution in NFs for 5 seconds (a) NF1, (b) NF2, (c) NF3, and (d) NF4.

Results indicate that the lower μ fluid leads to higher pressure increase rate, particularly within the NF1 and NF2. As the HF did not interact with the NF3 and NF4, no pressure increase is observed for these fractures.

4 CONCLUSIONS

In the research described here, the fully coupled lattice based 3D models were first compared with the findings of true triaxial fracturing experiments in the laboratory, and their corresponding CT scan and seismic velocity tomography analysis. As the similar NF/HF interaction mechanisms, particularly the arrest by NF1, and the subsequent crossing with offset on YD face, are captured well by the developed model, subsequent parametric studies were carried out to investigate the effects of fluid flow rate (q) and viscosity (μ) on NF/HF interaction. The results suggested that a higher q leads to a wider stimulated area with increased conductivities of rock and NFs. On the other hand, the obvious effects of μ could only be observed in the early stages of fluid injection, where the lower μ value is found to increase the conductivity at the near wellbore while the higher μ value resulted in a wider stimulated area. The pressure measured within NFs, indicating the NF dilation, also suggested that the higher pressure increment within major NFs is achieved with a lower μ.

ACKNOWLEDGEMENTS

The first author wishes to thank the Schlumberger Faculty for the Future Fellowship for the support she receives towards her research at Imperial College. She also thanks ITASCA for providing the XSite license through their Educational Partnership Program (IEP). The authors thank Karel Heller, Marc Friebel and Richard Bakker of Delft University of Technology and Graham Nash, Gary Jones and Harshit Agrawal of Imperial College London for their contributions to the laboratory experiments throughout the experimental research described in this paper. Part of the experimental work and data analysis reported in this paper were carried out with funding from the European Commission Research Fund for Coal and Steel (RFCS) project "Monitoring, Assessment, Prevention and Mitigation of Rock Burst and Gas Outburst Hazards in Coal Mines -MapROC", Grant No: RFCR-CT-2015-00005. The authors also wish to thank Alan Porter, the Assistant Quarry Manager at Hope Cement Works UK.

REFERENCES

Beugelsdijk LJL, CJ. De Pater, and K. Sato. 2000. Experimental hydraulic fracture propagation in a multi-fractured medium. In *SPE Asia Pacific Conference in Integrated Modeling for Asset Management, Yokohama, Japan.*

Chuprakov, D.A., O. Melcheava, and R. Prioul. 2013. Hydraulic Fracture propagation across a weak discontinuity controlled by fluid injection. In *Effective and Sustainable Hydraulic Fracturing*, ed. Andrew P. Bunger, John McLennan and Rob Jeffrey.

Damjanac, B., C.Detournay, P. Cundall, M. Purvance, and J.Hazzard. 2011. HF Simulator.

Damjanac, B., C.Detournay, P.A.Cundall, and Varun. 2013. Three dimensional numerical model of hydraulic fracturing in fractured rock masses.

Kresse, O., X.Weng, D.Chuprakov,R.Prioul, and C.Cohen. Effect of flow rate and viscosity on complex fracture development in UFM model. 2013. In *ISRM-ICHF, Brisbane,Australia.*

Li, B. 2014. Natural fractures in unconventional shale reservoirs in US and their roles in well completion design and improving hydraulic fracturing stimulation efficiency and production. *In SPE Annual Technical Conference and Exhibition, Amsterdam, The Netherlands.*

Mikada, H., J.Takekawa, J. 2015. The effects of fluid viscosity on the propagation of hydraulic fractures at the intersection of pre-existing fracture.

Nagel, N., I. Gil, M. Sanchez-Nagel., and B. Damjanac. 2011. The effect of operational parameters on hydraulic fracture propagation in naturally fractured reservoirs. In *SPE HFTC, Woodlands, Texas, USA.*

Wu, K. and J. E. Olson. 2014. Mechanics analysis of interaction between hydraulic and natural fractures in shale reservoirs-overcoming the limits of pseudo 3D models. In *URTEC Conference, Denver, Colorado, USA.*

Yildirim, B., W. Cao, S. Durucan, A. Korre, K.H.Wolf, R.Bakker, and A.Barnhoorn. 2018. The effect of natural fracture heterogeneity on hydraulic fracture performance and seismic response in shale and coal formations. In *2nd US Rock Mechanics/Geomechanics Symposium, American Rock Mechanics Association.*

Walton, I., and J.McLennan. 2013. The role of natural fractures in shael gas production In *International Society for Rock Mechanics and Rock Engineering.*

Yoon, J.S., A. Zang, O. Stephansson, H. Hofmann, and G. Zimmermann. 2017. Discrete element modelling of hydraulic fracture propagation and dynamic interaction with natural fractures in hard rock. *Procedia Engineering*. 191: 1023 – 1031.

Zhou, J., L. Zhang, Z. Pan, and H. Zhenhua. 2017. Numerical studies of interactions between hydraulic and natural fractures by smooth joint model. *Journal of Natural Gas Science and Engineering*. 46: 592-602.